Modeling and design of an electrically pumped SiGeSn microring laser

B. Marzban*[a], L. Seidel[b], V. Kiyek[c], T. Liu[c], M. Zöllner[d],
Z. Ikonic[e], G. Capellini[d], D. Buca[c], J. Schulze[f], M. Oehme[b], J. Witzens[a]
[a]Institute of Integrated Photonics, RWTH Aachen University, Aachen, 52074, Germany
[b]Institut für Halbleitertechnik, University of Stuttgart, Stuttgart, 70049, Germany
[c]Forschungszentrum Jülich GmbH, Jülich, 52428, Germany
[d]Leibniz-Institut für innovative Mikroelektronik GmbH (IHP), Frankfurt (Oder), 15236, Germany
[e]School of Electronic and Electrical Engineering, University of Leeds, Leeds, LS2 9JT, United Kingdom
[f]Lehrstuhl für Elektronische Bauelemente, Friedrich-Alexander-Universität Erlangen-Nürnberg, Erlangen, 91058, Germany

ABSTRACT

We present a suspended SiGeSn microring laser design that enables strain relaxation of the material layer stack, electrical pumping and adequate heat sinking. Using both strain and composition as two degrees of freedom to engineer the band structure, a direct bandgap is obtained in the gain material of a double heterostructure layer stack, and the L- to Γ-valley energy difference increased to 78 meV, by 66% compared to a non-underetched structure. The temperature dependent current threshold is modeled for the designed device and determined to be 18 kA/cm^2 at 50 K. The fabrication process is outlined and first experimental electroluminescence results indicating the effectiveness of our approach are reported. At the time this proceedings paper is being submitted, electrically pumped lasing has also been achieved with a similar structure, with results that will be reported in a future publication.

Keywords: (Si)GeSn, group IV lasers, microring lasers, strain engineering

1. INTRODUCTION

The (Si)GeSn alloy family has received a great deal of interest in recent years due to its direct bandgap, making group IV lasers possible [1]. Furthermore, this material platform covers a wide wavelength range from the short-wave to the long-wave infrared [2]. With these characteristics, (Si)GeSn alloys can be used in data communications, LiDAR, biochemical sensing, and eventually even quantum technologies [3].

Since GeSn's first demonstration as a direct bandgap material [4], laser diodes (LDs) [5,6], light emitting diodes (LEDs) [7,8], photodetectors (PDs) [9,10] and modulators [11] have been demonstrated. However, these devices are still in the proof-of-concept stage and each faces challenges if they are to be employed in real world scenarios. The SiGeSn LD, the main focus of this work, has been studied intensively in the last decade. A lot of progress has been made, even though the limited directness of the GeSn gain material, i.e., the L- to Γ-energy separation ($\Delta E_{L\Gamma}$), as well as the high dark recombination rates arising from a high density of point defects are still limiting the maximum lasing temperature and efficiency [12]. Experimentally, the LDs have been improved regarding their operating temperature [13,14] and lasing threshold [15]. Recently, the first electrically pumped laser has been demonstrated in a non-undercut Fabry-Perot configuration [16]. However, an efficient continuous wave (CW) electrically pumped room temperature (Si)GeSn laser is yet to be demonstrated.

In this paper, we present a novel electrically pumped (Si)GeSn laser design. The LD has a microring structure and is based on a double heterostructure (DHS) layer stack. In order to increase the directness in the active region, the whole layer stack is designed to be 910 nm thick, allowing partial relaxation. A GeSn buffer layer with a lower Sn-content than the active region is used at the bottom of the stack to prevent the misfit dislocations, resulting from relaxation, to reach the active region [6]. The microring is underetched on both sides, further increasing the directness by 31 meV. SiGeSn barrier layers are used on both sides of the GeSn active region to provide electrical confinement. The top SiGeSn layer is n-doped to

*fmarzban@iph.rwth-aachen.de; phone +49 241 80 20020; iph.rwth-aachen.de

Silicon Photonics XVII, edited by Graham T. Reed, Andrew P. Knights, Proc. of SPIE
Vol. 12006, 120060K · © The Authors. Published under a Creative Commons
Attribution CC-BY 3.0 License · doi: 10.1117/12.2609537

form a PIN diode and allows for carrier injection (the p-side of the diode relies on the intrinsic, defects based p-type doping at the bottom of the stack). The top electrode is recessed relative to the outer edge of the ring, with its position chosen as a trade-off between optical absorption of whispering gallery modes (WGM) travelling at the periphery of the disk and the diode's series resistance / required drive voltage.

The net gain is modeled in the following as a function of injected current in order to determine the temperature dependent lasing thresholds. Models and basic assumptions regarding material properties are the same as in [12]. First experimental results are shown for both a non-underetched and an underetched microring LD and compared with each other.

2. STRUCTURE DESCRIPTION AND MODELING RESULTS

The laser design is based on a 910 nm (Si)GeSn layer stack grown on a 2 µm p-doped ($1\times 10^{18}\mathrm{cm}^{-3}$) Ge virtual substrate (Ge-VS). To enable electrical connectivity, an n-doped barrier layer is grown on top of the active layer. The active layer and the underlying SiGeSn barrier layer are left undoped, but are assumed to be intrinsically p-doped [17], with different intrinsic doping levels modeled in the following. The modeled layer stack consists, bottom-to-top, of (i) a 170 nm $GeSn_{0.10}$ buffer layer, (ii) a 20 nm $Si_{0.080}GeSn_{0.080}$ barrier layer, (iii) a 640 nm $GeSn_{0.138}$ active layer, (iv) an n-doped $Si_{0.050}GeSn_{0.110}$ capping layer (60 nm 2×10^{18} cm^{-3} followed by 20 nm 5×10^{19} cm^{-3}). By means of the GeSn buffer layer, the remaining stack can be grown free of misfit dislocations, since the (Si)GeSn layer stack has a similar average lattice constant to that of the buffer [6]. Fig. 1(a) shows a cross-sectional scanning electron microscope (SEM) image of the sample overlapped with secondary ion mass spectrometry (SIMS) atomic distribution profiles. Given the thick layer stack, the active GeSn and SiGeSn barrier layers relax by 82% and 88%, respectively, as determined from an X-ray diffraction (XRD) reciprocal space map (RSM) of the layer stack, Fig. 1(b). The strain relaxation together with the 13.8% Sn composition of the gain medium ensure a direct bandgap active layer.

Using this layer stack, we evaluate three microring diode laser configurations, Fig. 2. In addition to the conventional microring laser shown in Fig. 2(a), we model undercut lasers in which an underetch is applied to the Ge-VS to both the outer and inner sides of the ring, Figs. 2(b) and 2(c). Furthermore, we study the effect of the conformal deposition of an additional SiN stressor layer on the strain and polarization dependent gain of the underetched structure, Fig. 2(c). The underetch by itself, even without the stressor layer, allows for mechanical extension of the undercut region, which reduces the compressive hydrostatic strain, increasing the directness ($\Delta E_{L\Gamma}$) of the gain material. The SiN layer further increases this deformation and can induce a net tensile strain, primarily along the radial direction. Uniaxial radial deformation can be problematic if the strain remains compressive along the azimuthal direction ($\varepsilon_{\theta\theta}$). The resulting gain coefficient will then favor optical amplification of light with an E-field also polarized along the azimuthal direction, as opposed to TE and TM WGMs that have their E-field either along the radial or vertical directions. Partial release of the membrane on both sides of the waveguide and deformation of the underlying pedestal, however, also allow some amount of biaxial deformation, alleviating this problem in the configurations shown in Figs. 2(b) and 2(c) [2]. The nominal design corresponds to a 1.75 µm underetch on both sides of the ring. With this, a 250 nm thick p-doped Ge layer remains on top of the silicon substrate as the hole transport layer, which is connected to the ring via a 1 µm wide pedestal.

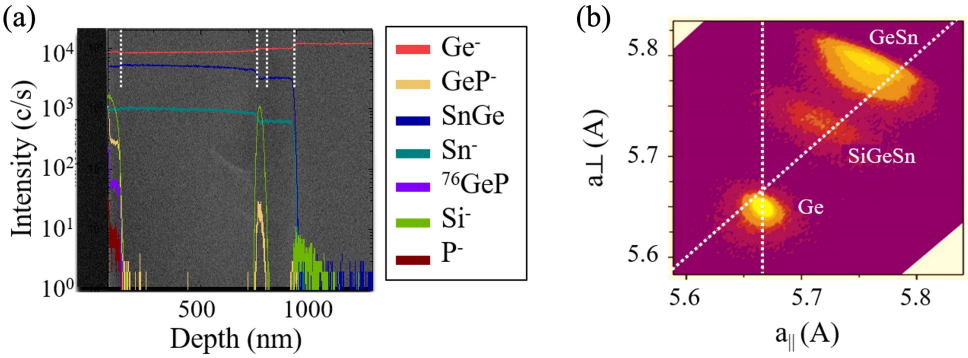

Figure 1. (a) Cross-sectional SEM image of the DHS layer stack overlaid with SIMS atomic distribution. (b) Reciprocal space map revealing the in- and out-of-plane lattice constants for the GeSn and SiGeSn layers. The GeSn and SiGeSn layer experience an 82% and 88% relaxation, respectively.

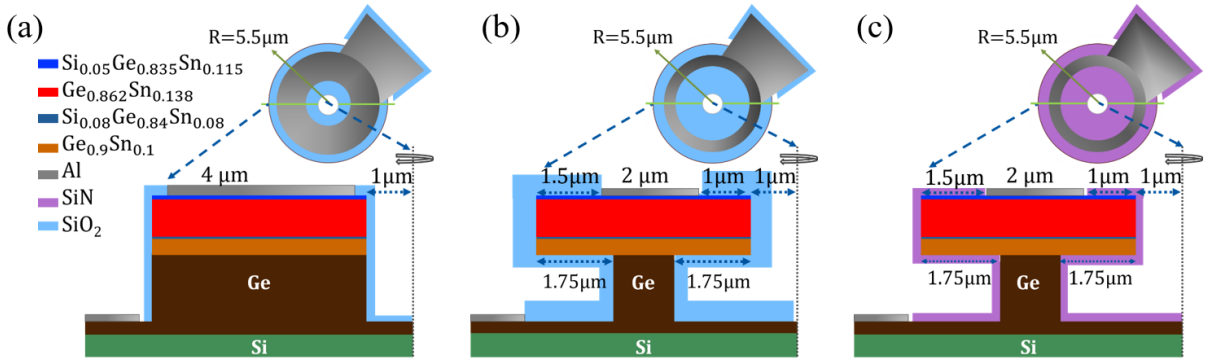

Figure 2. Microring laser configurations. (a) Non-underetched structure and (b), (c) underetched structures. The structure in (c) is provided with a conformally deposited, all-around SiN stressor layer.

In order to reduce optical absorption losses, the 2 μm wide top electrode is recessed 1.5 μm from the outer edge of the disk (R=5.5 μm). Fig. 3 shows the three lowest order TE and TM WGMs for the undercut structure shown in Fig. 2(b), in which the membrane is assumed to be clad by an 800 nm thick SiO_2 passivation and cladding layer. For both polarizations, the electric field of the ground mode (TE_0/TM_0) is close to zero at 1.5 μm from the periphery of the ring. Therefore, the electrode absorption losses for these modes are minimal. On the other hand, higher order modes will experience higher losses, as they come into contact with the top electrode. It should be noted that, from the perspective of the optical modes, the resonator behaves like a disk as the semiconductor film is sufficiently large for its inner sidewall not to interact with the light. Effective indices and losses are summarized in Table 1. While the two ground modes see negligible optical losses, the TM_2 mode experiences significant losses above 250 cm^{-1}. Modes with higher radial orders will experience even higher losses. Thus, by placing the top electrode away from the periphery, the lower order modes experience only small bending and absorption losses and have a higher chance of lasing. On the other hand, such placement of the electrode does reduce the current injection efficiency. As a benefit, this approach does not require thick, lower refractive index Ge or SiGeSn cladding layers to provide vertical light confinement, that remain challenging to grow. The bottom electrode is deposited on the remaining Ge-VS and is spaced 1.75 μm from the Ge pillar, flush with the outer circumference of the ring. The underlying Si is assumed to be undoped, so that the current has to flow through the Ge film.

To understand the carrier transport in these structures, their energy band diagrams first need to be modeled. For this, we first model the residual strain distribution. Then, by employing 8 band k·p theory, we model the band diagram given the

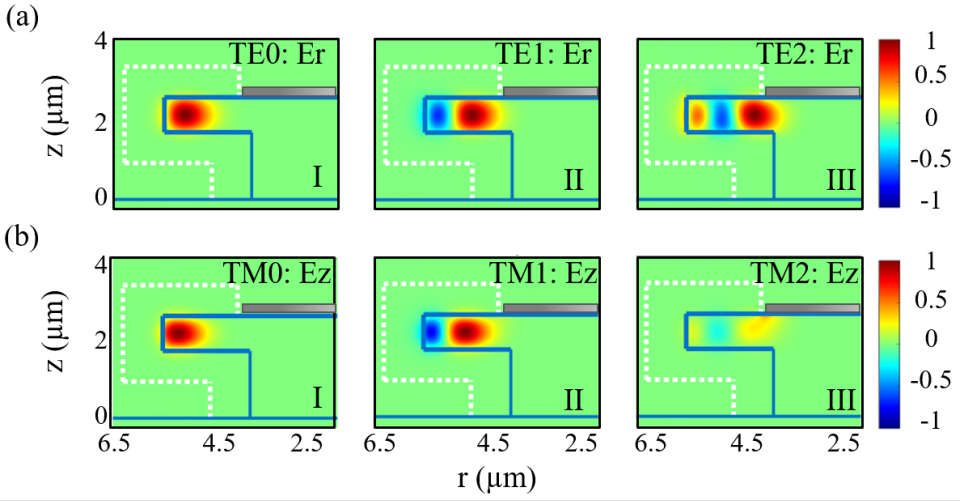

Figure 3. Mode profiles of the TE and TM whispering gallery modes. E-field components along (a) the radial direction for the TE_0, TE_1 and TE_2 modes and (b) the vertical direction for the TM_0, TM_1 and TM_2 modes. The increased higher-order modes' losses are due to their higher surface overlap with the top electrode.

material compositions and the strain profile. The strain profile is obtained through simulations in COMSOL's structural mechanics package. Before device fabrication, biaxial in-plane strain values $\varepsilon_{||} = (\varepsilon_{rr} + \varepsilon_{\theta\theta})/2$ equal to -0.27%, -0.11%, -0.37%, -0.17% are measured in the GeSn buffer layer, bottom SiGeSn barrier, GeSn active region, and top SiGeSn barrier, respectively. Moreover, a small tensile strain equal to 0.16% is observed in the Ge-VS. Using these in-plane strain values, the strain in the growth direction ε_{zz} (z-axis) is calculated for each region [18]. These strain values are then used as initial conditions for the residual strain profile calculations using COMSOL, in which the undercut structure is allowed to mechanically relax. We observe that with the underetch the structure bows slightly downwards, with the rim of the disk moving down by 26 nm relative to the center position. The residual strain is plotted along a vertical cut through the structure in Fig. 4(a), with $\varepsilon_{||}$ and ε_{zz} the in-plane and out-of-plane strain. The vertical cut is taken at a position close to the periphery, where the optical field of the TE and TM ground modes has its maximum. The residual strain is not strictly biaxial. For instance, in the middle of the GeSn active region ε_{rr} equals -0.017% and $\varepsilon_{\theta\theta}$ equals -0.070%, resulting in an average $\varepsilon_{||}$ of -0.044%. However, the difference between ε_{rr} and $\varepsilon_{\theta\theta}$ is rather small (0.053%) and only mildly impacts the isotropy of the gain for the in-plane (TE) E-field polarizations. We model the material gain for TE-polarized WGMs, with an E-field oriented along the radius of the ring, to be only 17% below the gain coefficient for light with the E-field polarized along the azimuthal direction. The residual strain profile is relatively homogenous inside the gain material, both along the growth (z-)direction, Fig. 4(a), and across the horizontal (xy) center-plane of the gain medium, Fig. 4(b).

With the underetch, although the structure relaxes, as explained above, a small residual compressive strain remains in the active region. The hydrostatic (average) strain can be further improved by using an all-around compressively strained SiN layer, that applies tensile stress to the semiconductor stack. Simulations indicate that tensile strain can even be obtained in the active region. Applying significant stress with the SiN layer in this way also leads to a strong anisotropy of the in-plane strain coefficients in the gain material, due to anchoring by the pedestal. For example, with the given underetch of 1.75 μm, a 250 nm thick, 2.7 GPa compressively strained SiN layer [19] would result in considerably different strain coefficients along the in-plane directions, with ε_{rr} equal to 0.337% and $\varepsilon_{\theta\theta}$ equal to 0.145%. However, with this net tensile in-plane strain ($\varepsilon_{||}$), the gain material will be compressively or very weakly tensile strained in the growth direction [19], resulting in significant gain for the TM polarization, also supporting WGMs. Application of the SiN layer on both the top and bottom surfaces of the ring allows to maintain a relatively homogeneous distribution of the strain across the gain medium, as in the undercut-only structure. Using only a top stressor, on the other hand, results in the structure bending further down, improving the isotropy of the tensile strain in the xy-plane. However, the magnitude of the strain will then vary much more along the growth direction, as a consequence of this deformation [6,12]. For instance, if the 2.7 GPa stressor layer mentioned above is deposited only on top of the layer stack, for example immediately after growth and before any further device processing, the strain ($\varepsilon_{||}$) will vary from -0.076% compressive at the bottom of the GeSn active region to 0.53% tensile at the top of the stack.

In this work, we mainly focus on modeling results for the underetched structure without SiN stressor layer shown in Fig. 2(b). In Fig. 4(c), the flat-band energy diagram (i.e., before applying dopants) is plotted along the growth direction given the residual strain levels shown in Fig. 4(a). These have been spatially averaged for each layer, approximating them as being homogeneous. In the active region, the bandgap is calculated as 0.45 eV, with the two SiGeSn barrier layers ensuring carrier confinement. The Γ-electrons see a ~300 meV and ~150 meV barrier at the interface with the bottom and top SiGeSn layers, respectively. The hole confinement is weaker, with heavy holes (HH) only experiencing a barrier height of ~90 meV and ~ 60 meV at the bottom and top SiGeSn barriers, respectively. We calculate a gain material directness of 78 meV, which is 66% higher than that of the non-underetched structure ($\Delta E_{L\Gamma} = 47$ meV). It is important to note that, as in [12], we have applied a 30 meV downward correction to the directness calculated from the bowing parameters taken from [20], as this has previously resulted in better consistency with experiments, see [12] for details.

Table 1. Effective index and losses for the three lower order modes for both polarizations.

	TE_0	TM_0	TE_1	TM_1	TE_2	TM_2
Effective Index	3.555	3.557	3.175	3.184	2.867	2.916
Loss (cm^{-1})	0.0015	0.0036	1.07	2.59	7.95	268

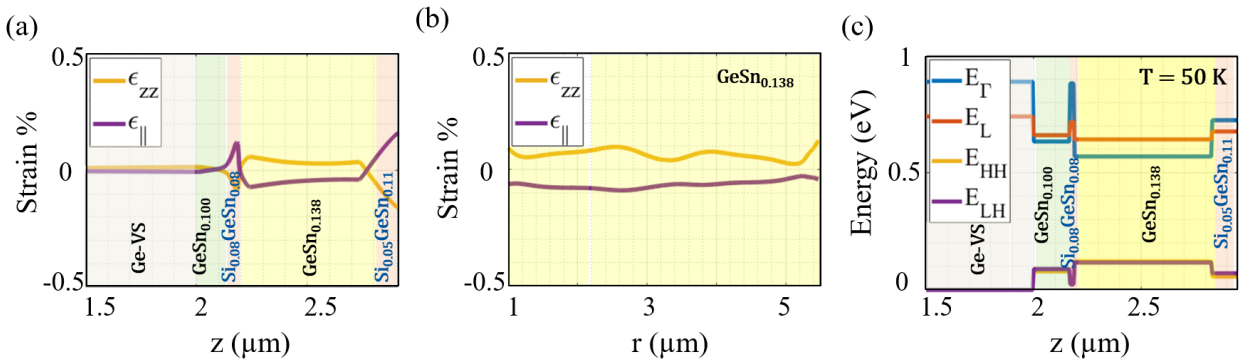

Figure 4. Strain profile and calculated energy diagram of the underetched structure. (a) Residual strain across the layer stack along the vertical axis near the periphery of the ring, where the optical field of the whispering gallery ground modes is maximal. (b) Residual strain in the middle of the GeSn active region, along the radius of the ring. (c) Flat-band energy diagram at 50 K. In the active region, with the underetch, a directness of 78 meV is calculated.

As a next step, we use the flat-band energy diagram, as shown in Fig. 4(c), to first calculate the voltage/current dependent carrier distributions and from them the photon energy dependent net gain. Carrier concentrations are modeled with help of the Synopsys Sentaurus Device (sDevice) toolbox as in [12]. We model a 2D cross-section of the structure corresponding to the diagram shown in Fig. 2(b). Material gain as well as free carrier absorption (FCA) losses corresponding to both intra-band transitions (empirically modified Drude model) and intervalence band absorption (IVBA) are then calculated from the carrier concentrations in a post-processing step. Furthermore, using the mode profiles shown in Fig. 3, we calculate the TE confinement factors of the TE_0 mode for the GeSn buffer, bottom SiGeSn barrier, GeSn active region, and top SiGeSn barrier to be 0.11, 0.03, 1.10, and 0.03, respectively. Similarly, the TM confinement factors of the TM_0 mode are 0.056, 0.024, 1.09, and 0.01 in these four regions. Fabrication driven scattering losses and self-heating

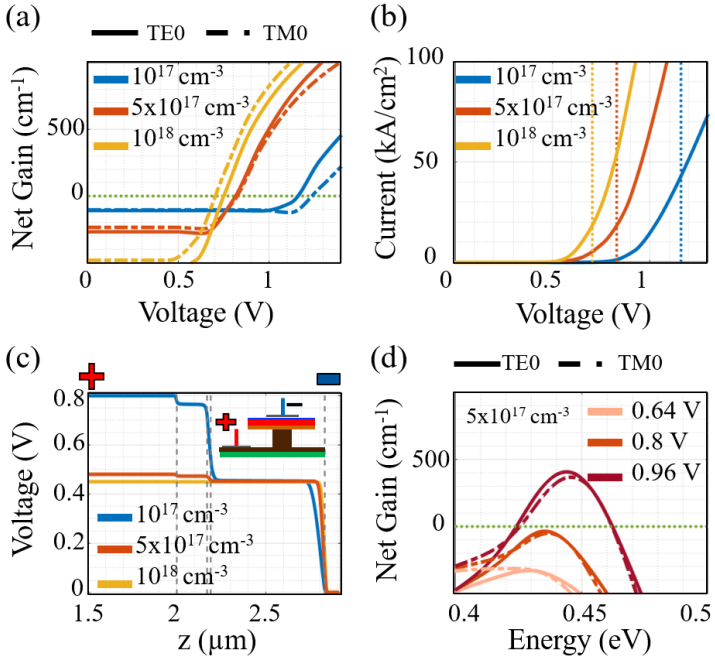

Figure 5. Modeling results for the underetched structure at 50 K for different p-type background doping assumptions. (a) Net gain as a function of applied voltage and (b) injected current density as a function of applied voltage. The dotted lines show the current densities required to reach threshold. (c) Voltage drop across a vertical cut in the middle of the structure when the diode turns on. The dashed lines show the border of each layer in the stack. (d) Net gain as a function of photon energy for a p-type background doping of 5×10^{17} cm^{-3} and different applied voltage levels. At threshold, the photon energy is modeled to be 0.44 eV.

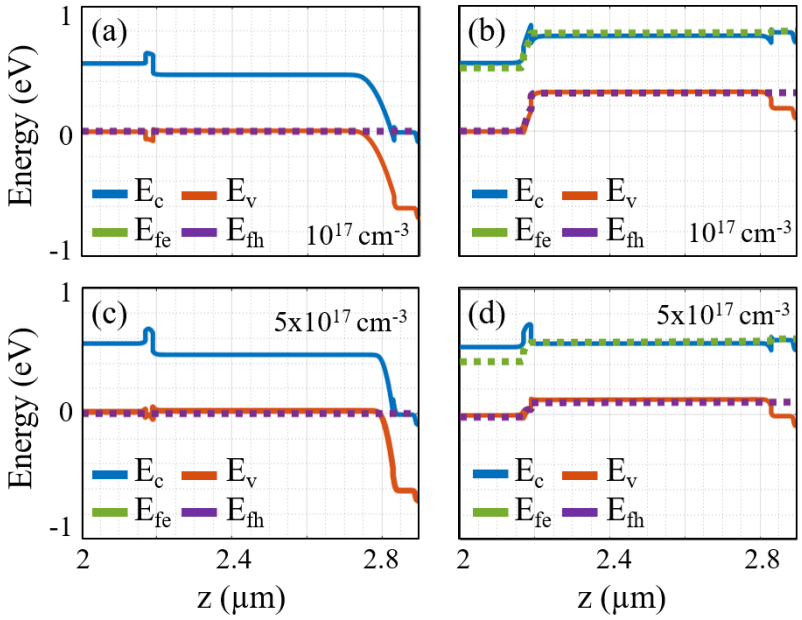

Figure 6. Band diagram at (a), (c) 0 V and at (b), (d) the diode turn-on voltage along a vertical cut through the structure at 50 K assuming an intrisnic p-doping of (a), (b) 10^{17} cm^{-3} and (c), (d) 5×10^{17} cm^{-3}. E_v (red), E_c (blue), E_{fh} (purple) and E_{fe} (green) are the valence band edge, conduction band edge, hole quasi-Fermi-level and electron quasi-Fermi-level.

of the device, that will be experimentally minimized by driving it with short pulses, are not considered at this point. Assumptions in regard to bowing parameters, carrier lifetimes, transition matrix elements etc. are taken from [12].

The net gain of the TE and TM ground modes, that see the lowest top electrode induced absorption losses, are then modeled as a function of the applied voltage and are plotted in Fig. 5(a). All modeling results are shown for a temperature of 50 K. Moreover, we study the effect of the p-type background doping level on the device performance by varying its value from 1×10^{17} cm^{-3} to 1×10^{18} cm^{-3}. We observe that a net zero gain will be first reached at 1.165 V by TE_0, 0.825 V by TE_0, and 0.705 V by TM_0, if the intrinsic doping is equal to 1×10^{17} cm^{-3}, 5×10^{17} cm^{-3}, and 1×10^{18} cm^{-3}, respectively. This can be further understood by examining the LD's current density versus voltage curves for the three considered intrinsic doping levels, Fig. 5(b). If the lowest, 1×10^{17} cm^{-3} p-type doping is considered in the GeSn buffer, bottom SiGeSn barrier and GeSn active region, the diode's turn-on voltage is ~0.8 V, considerably above the 0.45 eV bandgap of the active region. On the other hand, if the highest 1×10^{18} cm^{-3} p-type background doping is considered, the turn on voltage drops to ~0.5 V and is much closer to the expected value. The voltage drops along a vertical cut through the layer stack can be seen in Fig. 5(c). It is apparent that the expected 0.45 V drop occurs between the p-doped gain layer and the n-doped top barrier, as expected, but that an additional voltage drop builds up at the bottom barrier, as a consequence of the undesirable barrier to hole injection. This can be further understood with help of Fig. 6, that shows the band diagram along a vertical axis across the structure for the low (10^{17} cm^{-3}) and intermediate (5×10^{17} cm^{-3}) intrinsic p-doping levels, at 0 V and at the diode turn-on voltages. It is apparent in Fig. 6(a) that for the low doping level the lower SiGeSn barrier layer results in a substantial barrier for hole injection. On the other hand, higher p-doping levels flatten the valence band energy on this side of the diode, improving at the same time the electron confinement, see Fig. 6(c).

As the diode is turned on, this barrier to hole injection leads to an additional voltage drop across the lower barrier layer. It is, however, much lower at high doping levels for which this barrier has been weakened. At the turn-on voltage, adequate barriers can be seen for electrons and holes at the lower and upper barrier layers, respectively, for the higher doped structure (Fig. 6(d)). However, for the lower intrinsic doping level, the barrier confining electrons at the bottom of the gain material can be seen to be much weakened (Fig. 6(b)). For one, the conduction-band barrier energy is not pushed up by flattening of the valence band. In addition, an electron accumulation layer at the lower edge of the gain region bends the band diagram and further lowers the barrier energy. As a consequence, the electron quasi-Fermi-level is seen not to drop significantly below the conduction band edge in the GeSn buffer layer, the lowest structure shown in the diagram, pointing to a large

electron leakage current escaping the gain region. This is confirmed by the modeled LD threshold currents. With these three background doping levels, 1×10^{17} cm^{-3}, 5×10^{17} cm^{-3}, and 1×10^{18} cm^{-3}, the LD's threshold is modeled to be at a current density of 43 kA/cm^2, 18 kA/cm^2, and 17 kA/cm^2, respectively, defined as the current injected at the electrode (in kA/cm in the 2D simulation) divided by the width of the semiconductor strip. The strong increase of the required injection current at the lowest intrinsic doping level is due to the high electron escape current.

Since IV measurements carried out on the fabricated structures shown in the next section feature a turn-on voltage around 0.4 V at cryogenic temperatures, it is likely that the actual p-type background doping is significantly larger than 1×10^{17} cm^{-3} and in the 5×10^{17} cm^{-3} to 1×10^{18} cm^{-3} range. With the p-type background doping present in nominally undoped GeSn films being a sign of the material quality degradation, ideally as small as possible background doping is desired. Thus, ideally the active region would be intrinsic with the bottom buffer and barrier p-doped to act as hole transport and injection layers. Nevertheless, in the current structure the defects based background doping allows for hole transport in the bottom regions, in the absence of intentionally added p-doping. It should also be noted that, since self-heating and scattering losses are not considered here, experimental lasing thresholds are expected to be somewhat higher than modeled here.

Here, as in [12], we consider a bandgap narrowing equal to 24 meV at 50 K. With this, we model the net gain to reach zero at a photon energy equal to 0.44 eV for 5×10^{17} cm^{-3} background doping. This can be seen in Fig. 5(d), in which we plot the net gain as a function of energy for the TE_0 and TM_0 modes.

3. FABRICATION AND INITIAL EXPERIMENTAL RESULTS

We fabricate both non-underetched and underetched microrings in a single-mesa process. All semiconductor surface cleaning steps include treatment with acetone, isopropanol, an O_2-plasma, HF and HCl. For the underetched structure, after etching the mesa with an HBr-plasma, the underetch follows directly in the same inductively coupled plasma reactive ion etching (ICP-RIE) system using a CF_4-plasma. The SiO_2 passivation is deposited via plasma enhanced chemical vapor deposition (PECVD) using tetraethylorthosilicate (TEOS) as a precursor. Opening of the oxide windows is carried out with CF_4 and Ar in a reactive ion etching (RIE) system. In a last step, 2 µm of Al is sputtered and structured with an HBr-plasma in the ICP-RIE system.

In Fig. 7(a), the deformation after underetching of a test structure with a reduced 1.4 µm radius can be seen, in the form of a slight downward bowing allowing further relaxation of the layer stack. Figure 7(b) shows an SEM image of a LD that is very similar to the one discussed and modeled in the previous section, with underetching applied at both the inner and outer sidewalls of the ring. An additional mesa is patterned outside of the ring, that serves to route out the top electrode to the right, without the metal covering the periphery of the ring. The SEM image was taken after oxide deposition and sputtering of the Al electrodes. Prior to the deposition of the Al, openings have been patterned in the oxide on top of the disk for the top electrode contact as well as on top of the remaining Ge film in the form of an anulus sector seen on the left of the image for the bottom electrode contact.

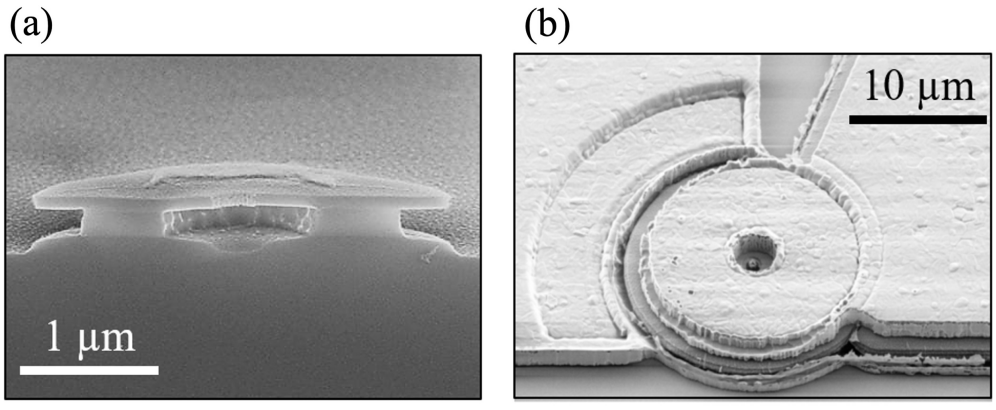

Figure 7. SEM images of fabricated structures. (a) Test structure with 1.4 µm radius. The downward bending of the membrane at the outer periphery of the ring can be observed. (b) Fabricated undercut microring after oxide deposition, opening and Al sputtering.

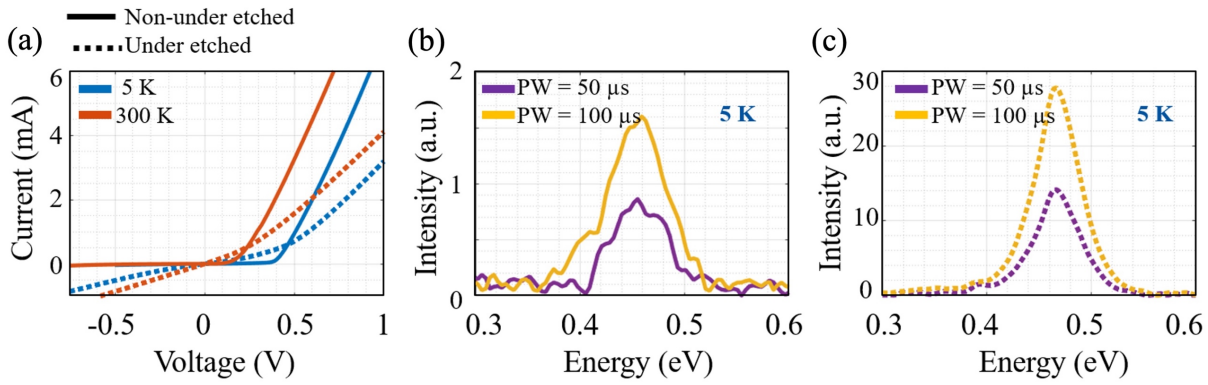

Figure 8. Initial experimental results of non-underetched and underetched microrings. (a) IV measurements of both structures at 5 K and 300 K. The non-underetched structure has lower forward resistance and reverse current. (b) EL measurement of non-underetched structure at 5 K with 72 kA/cm^2 current injection with 50 µs and 100 µs pulse widths. (c) EL measurement of underetched structure at 5 K with 22 kA/cm^2 current injection with 50 µs and 100 µs pulse widths.

We present initial experimental results for both a 5 µm radius non-underetched and underetched microring. First, we perform DC current-voltage (IV) measurements for both structures at 5 K and 300 K. Here we observe that the underetched structure exhibits substantially larger forward resistance than the non-underetched one. By underetching the ring, the height of the Ge slab through which the holes are injected from the positive contact is reduced, hence increasing the resistance. Additionally, the measured forward resistance is higher than the modeled one in both cases, which we attribute to the Ge-VS being p-doped less than the nominal 1×10^{18} cm^{-3} concentration. In particular, the doping of the Ge-VS was graded in the fabricated structure and is weaker in the bottom portion of the film used for carrier transport in the undercut structure, for which the modeled forward resistance of ~10 Ω is much smaller than the measured ~170 Ω at cryogenic temperatures. The non-underetched LD also has close to zero reverse current at negative bias voltages, while the underetched structure features substantial leakage currents.

We also carried out electroluminescence (EL) measurements of these two structures. The EL emission signal was collected and analyzed using a spectrometer with a liquid-nitrogen-cooled InSb detector (response range 1-5.5 µm). These initial measurements were performed with test equipment limited to the generation of relatively long pulses (> 50 µs), for which laser action was not observed due to substantial self-heating of the structures compounded by their higher than expected series resistance. The EL emission is shown for both structures at 5 K for pulse widths of 50 µs and 100 µs in Figs. 8(b) and 8(c). The non-underetched structure was pumped with a high current density of 72 kA/cm^2 in order to be able to detect a signal, while the underetched structure was pumped at 22 kA/cm^2. Taking this into account, we observe that the underetched structure's emission is ~50 times stronger than that of the non-underetched device. The increased directness of the undercut structure plays a partial role here, since at this low temperature the L-valley is modeled to have just 30% of the total electron population in the non-undercut structure at the 72 kA/cm^2 pump density. We thus also attribute the improvement in the EL to the fact that in the non-undercut structure the electrode is placed closer to the semiconductor stack with a smaller oxide spacer (~300 nm). Furthermore, it is recessed by a smaller amount relative to the ring's outer periphery (1 µm vs. 1.5 µm for the undercut structure). As a consequence, the optical absorption losses are larger and more of the light is blocked from reaching the detection system collecting it from the top. At the time of the submission of this proceeding paper, a similar undercut structure has also been shown to lase at lower pulse widths, which will be reported in a future publication. There, the increased directness of the undercut structure plays an important role in maintaining lasing action as the temperature of the structure is increased.

4. CONCLUSION AND REMARKS

We present the design, modeling and initial experimental data of an electrically pumped (Si)GeSn underetched microring laser concept. The structure is realized by patterning and undercutting a microring in a DHS (Si)GeSn layer stack. We increase the directness of the active region by 66% by adding an underetch on both sides of the ring. The net gain of the laser is calculated at 50 K as a function of the pump current density and reaches threshold at 18 kA/cm^2. The fabrication process is outlined and initial measurement results are also described. Since lasing was prevented in these first measurements by self-heating arising from the long pulse widths, characterization is now ongoing with shorter pulses

generated by an improved current source. A similar structure has been shown to lase with electrical injection and will be reported in a future publication.

5. ACKNOWLEDGEMENT

The authors gratefully acknowledge funding from the Deutsche Forschungsgemeinschaft (DFG) for project 299480227.

REFERENCES

[1] Wirths, S., *et al.*, "Lasing in direct-bandgap GeSn alloy grown on Si," *Nat. Photon.* 9(2), 88-92 (2015).
[2] Moutanabbir, O., et al., "Monolithic infrared silicon photonics: the rise of (Si) GeSn semiconductors," Appl. Phys. Lett. 118(11), 110502 (2021).
[3] Soref, R. A., *et al.*, "Simulations of nanoscale room temperature waveguide-coupled single-photon avalanche detectors for silicon photonic sensing and quantum applications," ACS Appl. Nano Mat. 2(12), 7503-7512 (2019).
[4] Ghetmiri, S. A., et al., "Direct-bandgap GeSn grown on silicon with 2230 nm photoluminescence," Appl. Phys. Lett. 105(15), 151109 (2014).
[5] Stange, D., et al., "Optically pumped GeSn microdisk lasers on Si," *ACS Photon.* 3(7), 1279-1285 (2016).
[6] Stange, D., *et al.*, "GeSn/SiGeSn heterostructure and multi quantum well lasers," *ACS Photon.* 5(11), 4628-4636 (2018).
[7] Stange, D., *et al.*, "Short-wave infrared LEDs from GeSn/SiGeSn multiple quantum wells," *Optica* 4(2), 185-188 (2017).
[8] Yu, S. Q., *et al.*, "Si based GeSn light emitter: mid-infrared devices in Si photonics," in *Proc. SPIE* 9367, 9367OR (2015).
[9] Xu, S., *et al.*, "Integrating GeSn photodiode on a 200 mm Ge-on-insulator photonics platform with Ge CMOS devices for advanced OEIC operating at 2 μm band," *Opt. Expr.* 27(19), 26924-26939 (2019).
[10] Talamas Simola, E., *et al.*, "CMOS-Compatible Bias-Tunable Dual-Band Detector Based on GeSn/Ge/Si Coupled Photodiodes," *ACS Photon.* 8(7), 2166-2173 (2021).
[11] Hsieh, Y. D., *et al.*, "Electro-absorption modulation in GeSn alloys for wide-spectrum mid-infrared applications," *Commun. Mater.* 2(1), 40 (2021).
[12] Marzban, B., *et al.*, "Modeling of a SiGeSn quantum well laser," *Photon. Res.* 9(7), 1234-1254 (2021).
[13] Chrétien, J., *et al.*, "GeSn lasers covering a wide wavelength range thanks to uniaxial tensile strain," *ACS Photon.* 6(10), 2462-2469 (2019).
[14] Zhou, Y., *et al.*, "Optically pumped GeSn lasers operating at 270 K with broad waveguide structures on Si," *ACS Photon.* 6(6), 1434-1441 (2019).
[15] Elbaz, A., *et al.*, "Ultra-low-threshold continuous-wave and pulsed lasing in tensile-strained GeSn alloys," *Nat. Photon.* 14(6), 375-382 (2020).
[16] Zhou, Y, et al. "Electrically injected GeSn lasers on Si operating up to 100 K." *Optica* 7.8, 924-928 (2020).
[17] Von den Driesch, N., "Epitaxy of group IV Si-Ge-Sn alloys for advanced heterostructure light emitters," Ph.D. thesis, Faculty of Mathematics, Computer Science and Natural Sciences, RWTH Aachen, (2017).
[18] Boztug, C., *et al.*, "Strained-germanium nanostructures for infrared photonics," *ACS Nano* 8(4), 3136-3151 (2014).
[19] Millar, R. W., *et al.*, "Extending the emission wavelength of Ge nanopillars to 2.25 μm using silicon nitride stressors," *Opt. Expr.* 23(14), 18193-18202 (2015).
[20] Rainko, D., *et al.*, "Investigation of carrier confinement in direct bandgap GeSn/SiGeSn 2D and 0D heterostructures," *Sci. Rep.* 8, 15557 (2018).